

# ExoMol line lists – LII. Line Lists for the Methylidyne Cation ( $\text{CH}^+$ )

Oliver Pearce, Sergei N. Yurchenko and Jonathan Tennyson\*

*Department of Physics and Astronomy, University College London, Gower Street, WC1E 6BT London, UK*

Accepted XXXX. Received XXXX; in original form XXXX

## ABSTRACT

Comprehensive and accurate rovibronic line lists for the  $X^1\Sigma^+$  and  $A^1\Pi$  states of  $^{12}\text{C}^1\text{H}^+$  and  $^{13}\text{C}^1\text{H}^+$  which should be applicable up to temperatures of 5000 K are presented. Available empirical potential energy curves and high-level *ab initio* dipole and transition dipole moment curves are used with the program LEVEL to compute rovibronic energy levels and Einstein  $A$  coefficients.  $\Lambda$ -doubling is incorporated into the energy levels and  $A$ -coefficients involving the  $A^1\Pi$  state using an empirical method. For  $^{12}\text{C}^1\text{H}^+$ , line positions are improved by using both laboratory and astronomical observational spectra as input to the MARVEL procedure. The  $^{12}\text{C}^1\text{H}^+$  line list contains 1505 states and 34 194 transitions over the frequency range of 0 – 33 010  $\text{cm}^{-1}$  ( $\lambda > 300$  nm). Comparisons with observed astronomical and laboratory spectra give very good agreement. The PYT  $\text{CH}^+$  line lists and partition functions are available from the ExoMol database at [www.exomol.com](http://www.exomol.com)

**Key words:** molecular data – opacity – planets and satellites: atmospheres – stars: atmospheres – ISM: molecules.

## 1 INTRODUCTION

The methylidyne cation,  $\text{CH}^+$ , was one of the first molecules, and the first molecular ion, to be detected in space (Dunham 1937).  $\text{CH}^+$  has since been found to be ubiquitous in interstellar space (Godard et al. 2023) where it has been observed both in absorption and emission in various cool environments (Neufeld et al. 2021; Krelowski et al. 2020; York et al. 2013; Naylor et al. 2010; Cernicharo et al. 1997; Gredel et al. 1993; Crawford 1989; Dunham 1937) which include protostellar disks (Thi et al. 2011), diffuse clouds (Crane et al. 1995) and lines of sight towards star-forming regions (Falgarone et al. 2010), with even routine detection from extra-galactic sources (Falgarone et al. 2017; Muller et al. 2017; Rangwala et al. 2011; Ritchey et al. 2015). In addition, strong  $\text{CH}^+ A^1\Pi - X^1\Sigma^+$  emission spectra have been observed in the red rectangle (post-asymptotic giant branch star HD 44179), see Hobbs et al. (2004) and references therein.

Astrophysical interest in  $\text{CH}^+$  has sparked many investigations; these include using its unique properties, which allow tracing of significant energy releases and interstellar turbulence (Vidal-García et al. 2022), and its importance in astrochemistry, particularly for helping to understand diffuse interstellar clouds.  $\text{CH}^+$  is thought to be a building block for the formation of organic molecules in interstellar space, principally through its role as an intermediary in reactions producing larger hydrocarbons (Barinovs & van Hemert 2004; Domenech et al. 2018), and molecules including  $\text{C}_2$ ,  $\text{CN}$ ,  $\text{CO}$  and  $\text{CH}$  (Hakalla et al. 2007). Furthermore, owing to its efficient destruction mechanisms (Gredel et al. 1993) and inherently reactive nature with species prevalent in its environment (most notably  $\text{H}$  and  $\text{H}_2$ ), it came as a great surprise when the abundance of the molecule was observed to exceed predictions by several orders of magnitude (Dalgarno 1976). This has stimulated significant investigation into the formation, destruction and abundance of  $\text{CH}^+$  over many years (Gredel et al. 1993; Valdivia et al. 2017; Falgarone et al. 2010; Gredel 1997; Wesson et al. 2010; Gredel 1997). While the primary formation mechanism and observed abundance of  $\text{CH}^+$  remain in question, some recent studies have begun to provide explanations that reduce the large discrepancy between calculation and observation (Faure et al. 2017; Godard et al. 2023).

Interest in  $\text{CH}^+$  has also motivated a number of laboratory studies. Its rovibronic spectrum (involving vibrationally and rotationally-resolved transitions between electronic states) has been widely studied (Hechtfisher et al. 2007; Hakalla et al. 2006; Dubois & Lefebvre 2004; Hechtfisher et al. 2002; Carrington & Softley 1986; Sarre et al. 1986; Carrington & Ramsay 1982; Grieman et al. 1981; Helm et al. 1982; Cosby et al. 1980; Douglas & Morton 1960; Douglas & Herzberg 1942; Botterud et al. 1973; Mueller 2010; Yu et al. 2018), most notably the  $A^1\Pi - X^1\Sigma^+$  ( $A-X$ ) system which covers transitions between the

\* Corresponding author: [j.tennyson@ucl.ac.uk](mailto:j.tennyson@ucl.ac.uk)

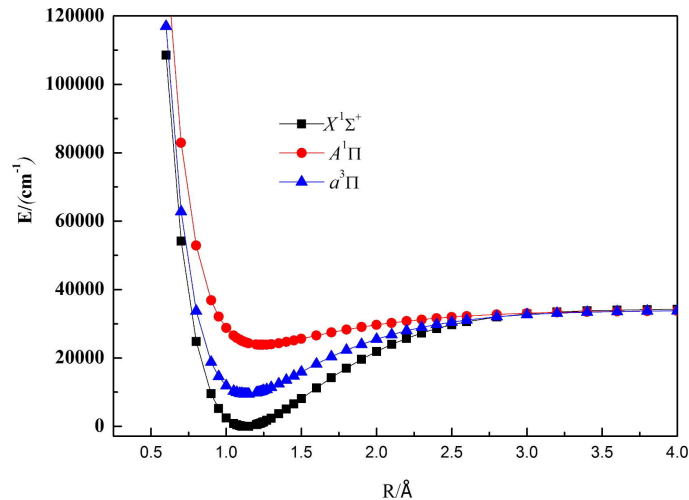


**Figure 1.** Potential energy curves for the low-lying electronic states below the first dissociation limit,  $X^1\Sigma^+$ ,  $A^1\Pi$  and  $a^3\Pi$ . Figure from Gao et al. (2017).

two lowest energy singlet states. Landmark studies include the work by Carrington & Ramsay (1982), the first high-resolution study (uncertainty  $\leq 0.01 \text{ cm}^{-1}$ ) which also assigned many transitions involving low vibrational levels ( $v'' = 0 - 3$ ), and more recently that of Hakalla et al. (2006) who comprehensively characterised low vibrational bands. The pure rotational spectrum of  $\text{CH}^+$ , first detected in space through emission lines from a planetary nebula (Cernicharo et al. 1997), has received much less coverage with only a few low-energy lines being observed so far. The first laboratory detection of a pure rotational line ( $J = 1 - 0$ ) (Pearson & Drouin 2006) was later proven to be inaccurate by  $0.0019 \text{ cm}^{-1}$  and its frequency was superseded by later studies (Domenech et al. 2018; Amano 2010b). The rovibrational spectrum has proven more elusive still, the first and only high resolution laboratory study was made by Domenech et al. (2018), and the corresponding astronomical detection only from one source, NGC 7027 (Neufeld et al. 2021). The minor isotopologues, most notably  $^{13}\text{CH}^+$  and  $^{12}\text{CD}^+$ , have also received significant spectroscopic investigation (Domenech et al. 2018; Bembenek et al. 1987; Amano 2010b; Dubois & Lefebvre 2004; Amano et al. 2015; Hechtfisher et al. 2007; Yu et al. 2018; Bembenek 1997). A summary of the spectroscopic laboratory and astronomically observed literature used in this study that covers the relevant electronic states,  $X^1\Sigma^+$  and  $A^1\Pi$ , is given in Table 1. Some papers provide spectroscopic analysis but do not present new line data (Amano 2010a; Yu et al. 2018; Amano 2015; Mueller 2010; Hakalla et al. 2007).

Theoretical investigations have aimed to characterise the potential energy curves (PECs) and dipole/transition dipole moments (DMs/TDMs) of  $\text{CH}^+$ . PECs, unique to each electronic state, describe the potential energy of an electron as a function of nuclear distance, while DMs/TDMs describe the strength of interaction between two different states during a transition between them. Many *ab initio* electronic structure studies have focused on  $\text{CH}^+$  since it contains just six electrons; these provide PECs for low-lying electronic states, notably  $X^1\Sigma^+$ ,  $A^1\Pi$  and  $a^3\Pi$  (Changala et al. 2021; Gao et al. 2017; Sauer & Spirko 2013), with some also characterising higher energy states (Mbiba Touedebe et al. 2023; Babb & McLaughlin 2017; Biglari et al. 2014; Barinova & van Hemert 2004; Kowalski & Piecuch 2001; Kanzler et al. 1991; Saxon et al. 1980). Here we use the PECs due to Cho & Le Roy (2016) who used a fully empirical (‘direct potential fit’) approach that utilises experimental data to fit the PECs of the  $X^1\Sigma^+$  and  $A^1\Pi$  states which, if sufficient experimental data is available, is a more accurate method than *ab initio* studies. The PECs of the three lowest electronic states of  $\text{CH}^+$  can be seen in Fig. 1 (Gao et al. 2017). Several studies have characterised DMs/TDMs (Changala et al. 2021; Gao et al. 2017; Babb & McLaughlin 2017; Sauer & Spirko 2013; Kanzler et al. 1991; Saxon et al. 1980) with notable investigations covering a vast number of singlet, triplet and quintet states using large basis sets and extending to large internuclear separations (Mbiba Touedebe et al. 2023; Biglari et al. 2014; Chakrabarti et al. 2017). The curves were compared (where data was available) and were seen to agree well, particularly those of A-X. A comparison of the X-X and A-A DMs and A-X TDMs from Biglari et al. (2014) and Changala et al. (2021) is shown in Fig. 2.

The ExoMol project aims to provide comprehensive spectroscopic data for transitions within molecules relevant to exoplanetary atmospheres, cool stars and brown dwarfs (Tennyson & Yurchenko 2012). Since its inception, the project has created line lists for many diatomic molecules, ions and larger polyatomic species, that comprehensively characterise the spectroscopic properties of the molecule and allows a model/profile to be built up. In this study, we calculate a comprehensive and accurate line list for the  $X^1\Sigma^+$  and  $A^1\Pi$  states of  $^{12}\text{C}^1\text{H}^+$  and  $^{13}\text{C}^1\text{H}^+$  as part of the ExoMol project.

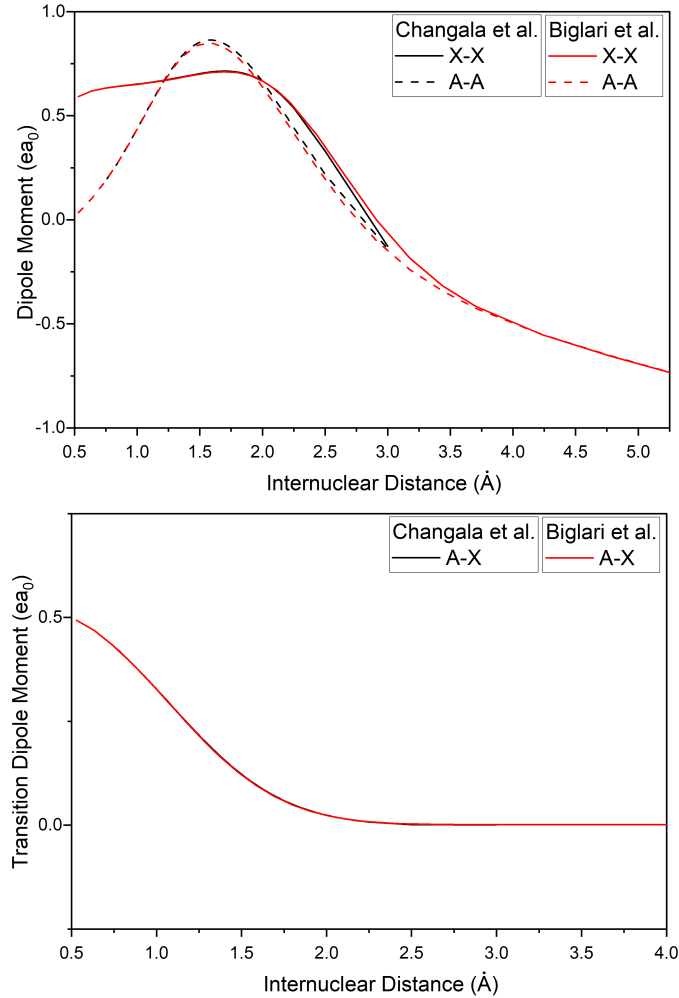


**Figure 2.** Comparison of dipole moments, in a.u., for the  $X^1\Sigma^+$  and  $A^1\Pi$  states (Top) and transition dipole moments for  $A^1\Pi - X^1\Sigma^+$  (Bottom) from Biglari et al. (2014) and Changala et al. (2021).

## 2 METHODS

To calculate the line list of  $\text{CH}^+$ , quantum mechanical nuclear-motion calculations were performed using the program LEVEL (Le Roy 2017) which generated the desired energy levels and transition data. To verify and improve on the calculated data, existing experimental and observational spectroscopic data for  $\text{CH}^+$  were gathered for use with the program MARVEL (Measured Active Rotational-Vibrational Energy Levels) (Furtenbacher et al. 2007). The MARVEL (Furtenbacher et al. 2007) algorithm inverts transition data to give highly accurate energy levels along with determined uncertainties.

### 2.1 MARVEL energy levels

767  $^{12}\text{CH}^+$  lines were collected from existing observational studies as summarised in Table 1. While most of the sources are from high resolution laboratory studies, 97CeLiGoCo (Cernicharo et al. 1997) and 21NeGoChFa (Neufeld et al. 2021) are actually astronomical observations. Table 1 shows that there are rather few observed transitions within the  $X^1\Sigma^+$  ground state of  $^{12}\text{CH}^+$ , hence the need to include astronomically observed lines which were deemed sufficiently accurate to use and helped to expand and refine the MARVEL network. The vast majority of existing data covers the A-X band with variable accuracy, with some papers, particularly older ones, not providing uncertainties at all and, in the case of 80CoHeMo (Cosby et al. 1980), not assigning their transitions. This means that the observed frequencies cannot be added to the MARVEL network, where the nodes are characterised by the quantum numbers of the energy levels involved. There is only comprehensive MARVEL energy level data (extending up to high  $J$ ) for vibrational states with  $v = 0 - 3/4$  for both electronic states, and some limited data for  $A^1\Pi v = 11 - 14$ .

MARVEL analyses uncertainty when evaluating transition data and is able to determine whether or not an uncertainty is consistent with the other data. Using this, the quoted experimental uncertainties for the older sources 42DoHe (Douglas &

**Table 1.** Summary of spectroscopic laboratory and astronomically observed papers used in our MARVEL study.

Reference	Freq. Range (cm <sup>-1</sup> )	Detected Transitions <sup>a</sup>	A/V <sup>b</sup>	Uncert <sup>c</sup> (cm <sup>-1</sup> )
21NeGoChFa (Neufeld et al. 2021)	2422.62 – 2942.57	(1, 0): $J'' \leq 10$	16/16	$3 \times 10^{-2}$
18DoJuScAs (Domenech et al. 2018)	27.85719 2711.81 – 2817.23	(0, 0): R(0) (1, 0): $J'' \leq 3$	5/5	$2 \times 10^{-5}$
15YuDrPeAm (Amano et al. 2015)	55.68 – 83.44	(0, 0): R(1), R(2)	2/2	$3 \times 10^{-6}$
10Amano (Amano 2010b)	27.85719	(0, 0): R(0)	1/1	$7 \times 10^{-7}$
06PeDr (Pearson & Drouin 2006)	27.85523	(0, 0): R(0)	1/0	$3 \times 10^{-6}$
06HaKeSzZa (Hakalla et al. 2006)	20401.56 – 23967.41	(0, 0), (0, 1), (2, 1): $J'' \leq 17$	124/124	$1 \times 10^{-2}$
02HeWiLaLi (Hechtfisher et al. 2002)	31747.0 – 33000.0	(11, 0), (12, 0), (13, 0), (14, 0): $J'' \leq 9$	35/35	1
97CeLiGoCo (Cernicharo et al. 1997)	55.68 – 165.92	(0, 0): $J'' = 1 - 5$	6/6	$5 \times 10^{-2}$
89SaWhGr (Sarre et al. 1989)	16750 – 18613	(0, 1), (1, 1), (2, 1): $J'' = 32 - 35$	6/6	1
86SaWaWh (Sarre et al. 1986)	16125.31 – 18613.07	(0, 0), (0, 1), (1, 1), (1, 2), (2, 1), (2, 2), (3, 2), (3, 3), (4, 3), (5, 3), (5, 4), (7, 4), (7, 5): $J'' = 18 - 35$	29/29	$5 \times 10^{-3}$
82CaRa (Carrington & Ramsay 1982)	17111.40 – 25281.30	(0, 0), (0, 1), (1, 0), (1, 1), (1, 2), (1, 3), (2, 1), (3, 1): $J'' \leq 14$	231/231	$1 \times 10^{-2}$
82HeCoGrMo (Helm et al. 1982)	15460 – 28484	Many $v' \leq 10$ vibrational bands: $J'' = 11 - 36$	51/51	1
81GrBrOkWi (Grieman et al. 1981)	22540.0 – 23615.1	(0, 0): $J'' = 6 - 21$	36/36	$1 \times 10^{-1}$
80CoHeMo (Cosby et al. 1980)	27494 – 28523	Transitions unassigned	N/A	$1 \times 10^{-2}$
60DoMo (Douglas & Morton 1960)	20524.30 – 26266.21	(0, 1), (1, 1), (2, 1), (3, 1), (4, 1): $J'' \leq 15$	130/129	$5 \times 10^{-2}$
42DoHe (Douglas & Herzberg 1942)	20636.8 – 26704.1	(0, 0), (0, 1), (1, 0), (2, 0): $J'' \leq 11$	94/94	$2 \times 10^{-1}$

<sup>a</sup> Bracketed values indicate the vibrational bands involved in transition, ( $v'$ ,  $v''$ ).

<sup>b</sup> 'A/V': Number of actual lines in source/Number of lines validated by MARVEL.

<sup>c</sup> Uncert: Average uncertainty as quoted (if available), or the modified uncertainty for the MARVEL algorithm.

Herzberg 1942), 60DoMo (Douglas & Morton 1960) and 81GrBrOkWi (Grieman et al. 1981) were increased to allow MARVEL to become self-consistent. After this it was only necessary to exclude two lines from the network: the 06PeDr pure rotational line and the 60DoMo A-X  $v = 2 - 1$  P(8) line.

The MARVEL input transitions file and output energies file are given as supplementary data to this paper. There was insufficient spectroscopic data to perform a MARVEL study for  $^{13}\text{CH}^+$ .

## 2.2 Calculations (LEVEL)

Version LEVEL-16 (Le Roy 2017) was used to compute the line list. This solves the radial Schrödinger equation to give vibrational and rotational energy levels within a defined potential, as well as transition frequencies and Einstein coefficients for the coupling within or between potentials. LEVEL was chosen as the existing work on  $\text{CH}^+$  by Cho & Le Roy (2016) used features in this program that are not easy to reproduce with other nuclear motion programs.

The effective radial Schrödinger equation used in this study as given by Cho & Le Roy (2016) is

$$\left\{ -\frac{\hbar^2}{2\mu} \frac{d^2}{dr^2} + V_i(r) + \frac{[J(J+1) - \Lambda^2] \hbar^2}{2\mu r^2} [1 + g_i(r)] \right\} \psi_{v,J}(r) = E_{v,J} \psi_{v,J}(r) \quad (1)$$

where  $\mu$  is the reduced mass and  $\Lambda$  represents the projection of electronic orbital angular momentum on the internuclear axis.  $V_i(r)$  is the adiabatic PEC of electronic state  $i$  that can include Born-Oppenheimer breakdown (BOB) functions and  $g_i(r)$  describes centrifugal BOB function; see Cho & Le Roy (2016) for more detail on these BOB functions. For the ( $\Lambda = 1$ ) A  $^1\Pi$  state, Cho & Le Roy also include a  $J$ -dependent term in the potential to incorporate the effects of  $\Lambda$ -doubling, as follows

$$sg(e/f)\Delta V_\Lambda(r) [J(J+1)]^\Lambda = sg(e/f) \left\{ \left( \frac{\hbar^2}{2\mu r^2} \right)^{2\Lambda} f_\Lambda(r) \right\} [J(J+1)]^\Lambda \quad (2)$$

where  $sg(e/f) = +1$  and  $0$  for  $e$  and  $f$  levels respectively (in accordance with the form suggested later by Yu et al. (2018)), and  $f_\Lambda(r)$  is a  $\Lambda$ -doubling radial strength function with the following form, also determined by Cho & Le Roy

$$f_\Lambda(r) = \sum_{i=0}^4 \omega_i y_{p_\Lambda}^i \quad (3)$$

with

$$y_{p_\Lambda}(r) = \frac{r^{p_\Lambda} - r_e^{p_\Lambda}}{r^{p_\Lambda} + r_e^{p_\Lambda}} \quad (4)$$

where  $\omega_i$  are expansion coefficients,  $r_e = 1.235896 \text{ \AA}$  is the equilibrium internuclear distance for the A <sup>1</sup>Π state potential, and  $p_\Lambda = 4$ , all determined and given in Cho & Le Roy (2016). Solving Eq. (1) for each of the two electronic state potentials,  $V_i(r)$ , yields the vibrational and rotational eigenfunctions (energy levels) that form the basis of the line list.

### 2.2.1 Potential Energy and Dipole Moment Curves

The CH<sup>+</sup> input file created for use in LEVEL by Cho & Le Roy (2016) was used as a basis in this study. Our investigation was limited to the ground and first excited singlet states, X <sup>1</sup>Σ<sup>+</sup> and A <sup>1</sup>Π, as investigated by Cho & Le Roy. As shown in Fig. 1 these are the only singlet states below the first dissociation limit, and any spin-forbidden transitions between these states and the low-lying triplet (a <sup>3</sup>Π) state are yet to be observed and likely to be extremely weak (Gao et al. 2017). Spin-orbit coupling to this state was also neglected.

The full, empirical potential energy curves calculated by Cho & Le Roy (2016) utilise previous spectroscopic data to characterise the curves more accurately than previous *ab initio* studies. Literature DMs (X-X and A-A) and TDMs (A-X) were compared to determine the most suitable available dipole moment curves, see Fig. 2. Since all curves agree well, we chose those of Biglari et al. (2014), due to their comprehensive characterisation of the curves up to high internuclear distance,  $r$ . We note that Mbiba Touedebe et al. (2023) also recently characterised these quantities, but their work only became available after we started calculations and hence was not considered in the initial analysis.

To get correct results it transpired that the basic input file provided by Cho & Le Roy (2016) required modification. We utilised the most recent version of LEVEL (LEVEL-16) but there were significant issues with the both input file and the LEVEL code itself. Firstly, the input file gave incorrect values for several parameters which had to be investigated and corrected. For example,  $\Lambda$  being set to 0 for the A <sup>1</sup>Π and most of the parameters describing the <sup>12</sup>CH<sup>+</sup> X <sup>1</sup>Σ<sup>+</sup> ground state were set to values that describe the <sup>12</sup>CD<sup>+</sup> A <sup>1</sup>Π excited state! Even when amended, the input file still gave errors when running with LEVEL. Analysis of the Fortran source code showed that in places the code disagreed with the documentation and input file structure on the ordering of parameters that read the input potential energy function; we therefore modified the LEVEL code to resolve these errors. As Cho & Le Roy (2016) did not consider transition probabilities, we then modified the input file to read in the DM/TDM functions and to instruct LEVEL to compute Einstein A coefficients. The final version of the LEVEL input file is provided as supplementary info. The source for the modified LEVEL can be found at [github.org/exomol](https://github.org/exomol).

### 2.2.2 $\Lambda$ -Doubling

LEVEL does not consider  $\Lambda$ -doubling, the splitting of rotational energy levels in  $\Lambda > 0$  electronic states due to their  $e/f$ -parity.  $\Lambda$ -doubling is an important effect to consider, as without it our calculated energy levels in the A <sup>1</sup>Π state would be degenerate which is incorrect. Yu et al. (2018) analysed  $\Lambda$ -doubling in the CH<sup>+</sup> A <sup>1</sup>Π state where the effect arises due to the interactions of the  $e/f$  rotational levels with <sup>1</sup>Σ<sup>+</sup>/<sup>1</sup>Σ<sup>-</sup> states, respectively. They found that treatment of this effect in all previous spectroscopic studies was incorrect as it was generally assumed that the  $\Lambda$ -doubling energy of  $e/f$  levels would lead to a symmetric shift in their energy terms, as the magnitude of the interaction of  $e$  levels with Σ<sup>+</sup> states and  $f$  levels with Σ<sup>-</sup> states was assumed to be equal. In practice, Yu et al. (2018) argued that the energy splitting is asymmetric with the  $f$  levels negligibly perturbed since Σ<sup>-</sup> states will lie at much higher energy (none have so far been detected). In accordance with the findings of Yu et al. (2018), the A <sup>1</sup>Π state energies computed by LEVEL correspond to the energy of the unperturbed  $f$ -parity level. It is therefore necessary to account for the perturbed  $e$ -parity levels. Cho & Le Roy (2016) model the splitting by the inclusion of an additional term in the potential energy function of their radial Schrödinger equation, as described in Eq. (2), which shows that the  $e$ -parity energy level perturbation increases with  $J^2$ , whereas the  $f$ -parity levels are unperturbed. Since the version of LEVEL we used does not account for this, an empirical approach to considering the effect was taken.

The approach taken consisted of separately calculating a correction to each  $f$ -parity rotational level within each vibrational level of the A <sup>1</sup>Π state, which could be applied to give the energy of the corresponding  $e$ -parity level. This involved computing the expectation value of the operator  $\Delta V_\Lambda(r)$  given in Eq. (2) for each vibrational level,  $\langle \psi_v | \Delta V_\Lambda(r) | \psi_v \rangle$ , and evaluating the rotational  $J$ -dependence to give the energy level correction. To do this, the operator was calculated for each value of internuclear distance,  $r$ , in steps of 0.001  $\text{\AA}$  from  $r_{\min}$  to  $r_{\max}$  for each vibrational level, which ranged from 2100 grid points for  $v = 0$  to 90 000 for  $v = 14$ . The value of the vibrational wavefunction, provided by LEVEL upon modification of the input file, was also gathered at each value of  $r$ . The expectation value,  $\langle \psi_v | \Delta V_\Lambda(r) | \psi_v \rangle$ , was then calculated for each  $r$  value and these were summed to give the overall expectation value for that vibrational level. This was repeated for all vibrational levels, and these values can be seen in column 2 of Table 2. Incorporating the  $J$  dependence by evaluating the entirety of Eq. (2) (multiplying these corrections by  $J(J+1)$ ) gave the correction for each rotational level within each vibrational level. These corrections were then simply added to the  $f$ -parity energy to obtain the perturbed  $e$ -parity energy.

To verify these calculations, comparison was made to observed (experimental) splittings, some of which were available from MARVEL data (where both  $e$  and  $f$  energies for the same rotational level were known). The calculations did not initially produce results in line with observational corrections, however, further investigation revealed that the ratio between the calculated and

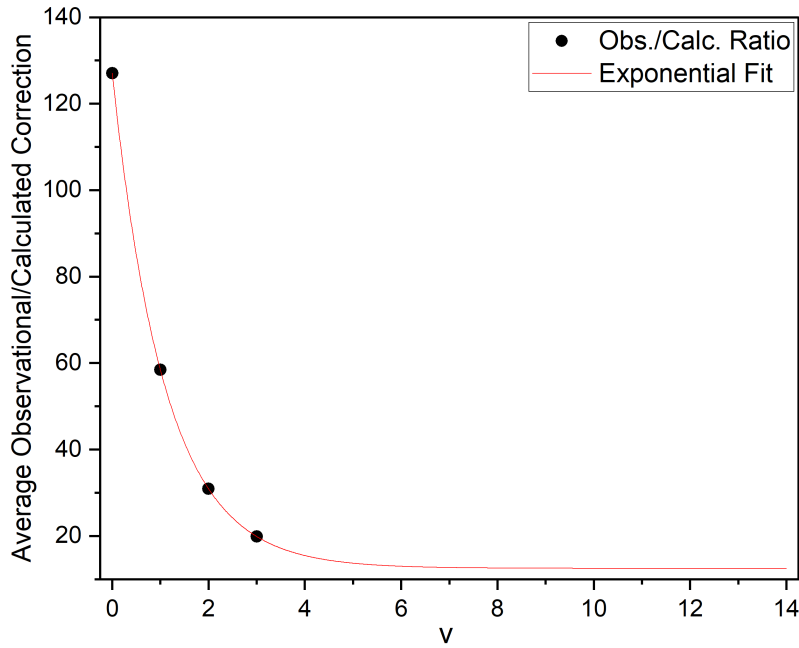


**Figure 3.** The average ratio of observed to calculated  $\Lambda$ -doubling correction ( $e - f$  energy) plotted against vibrational level. An extrapolation to higher vibrational levels is performed using an exponential fit. Values of average ratio can be seen in Table 2 for all  $v$  levels.

**Table 2.**  $\Lambda$ -doubling correction calculation parameters, showing the original expectation value of the  $\Lambda$ -doubling operator for each vibrational level, the observed/calculated correction ratio and the resulting scaled calculated correction. Asterisks indicate extrapolated ratios.  $J$ -dependence can then be incorporated by evaluating the entirety of Eq. (2) using the scaled values to give the final correction to each  $f$ -state energy to account for  $\Lambda$ -doubling.

$v$	Original $\langle \psi_v   \Delta V_\Lambda   \psi_v \rangle$ (cm-1)	Average Obs./Calc. Ratio	Scaled $\langle \psi_v   \Delta V_\Lambda   \psi_v \rangle$ (cm-1)
0	0.000297	127.051	0.037787
1	0.000594	58.449	0.034727
2	0.001017	30.897	0.031434
3	0.001429	19.902	0.028440
4	0.001736	15.464*	0.026851
5	0.001906	13.690*	0.026096
6	0.001946	12.978*	0.025261
7	0.001877	12.693*	0.023827
8	0.001713	12.579*	0.021553
9	0.001463	12.533*	0.018334
10	0.001134	12.515*	0.014188
11	0.000752	12.507*	0.009402
12	0.000384	12.504*	0.004800
13	0.000136	12.503*	0.001704
14	0.000026	12.503*	0.000322

corresponding observed correction was generally constant within each vibrational level from  $v = 0$  to  $v = 3$ , the region over which the MARVEL data was fairly comprehensive. Therefore the calculated corrections within each vibrational level could be scaled by the average ratio to provide an accurate account of  $\Lambda$ -doubling in line with observation. The average ratio for each  $v$  can be seen in Fig. 3, showing an apparent exponentially-decaying trend with increasing  $v$ . Unfortunately, due to the limited coverage of the MARVEL data, little information about higher  $v$  levels meant an extrapolation of the curve was necessary to estimate the ratio for higher  $v$  levels. The extrapolation was performed using an exponential fit and is shown in Fig. 3. From this, the extrapolated ratio for  $v \geq 4$  levels could be estimated, as seen by the asterisked values in column 3 of Table 2. With this, the calculated corrections for each level were scaled by the corresponding ratio to give the final correction for each  $v$  level, as can be seen in the final column of Table 2. After applying  $J$ -dependence, the final correction values for each level was added to the corresponding ( $f$ -state) energy to give that of the  $e$ -state. The scaling with observational corrections means this approach should be accurate for low  $v$ 's but the extrapolated corrections are less secure and would benefit from experimental confirmation.

### 2.2.3 Einstein Coefficients

LEVEL computes Einstein  $A$  coefficients using the expression

$$A_{v',J',v'',J''} = 3.1361891 \times 10^{-7} \frac{S(J',J'')}{2J'+1} \nu^3 |\langle \Psi_{v',J'} | M(r) | \Psi_{v'',J''} \rangle|^2 \quad (5)$$

where  $A$  is the Einstein coefficient (s<sup>-1</sup>),  $S(J',J'')$  is the Hönl-London rotational intensity factor (Hansson & Watson 2005),  $J'$  the upper level rotational quantum number,  $\nu$  the transition wavenumber (cm<sup>-1</sup>),  $\Psi_{v',J'}$  and  $\Psi_{v'',J''}$  the normalised initial and final state radial wavefunctions and  $\langle \Psi_{v',J'} | M(r) | \Psi_{v'',J''} \rangle$  the expectation value of the dipole/transition dipole moment function  $M(r)$ , which we asked LEVEL to output.

LEVEL's lack of consideration of  $\Lambda$ -doubling means  $e$ -parity A<sup>1</sup>Π levels are not present and transitions involving these states were not correctly accounted for. A<sup>1</sup>Π( $e$ )-X transitions were incorrectly assigned the wavenumber of the corresponding (forbidden by dipole selection rules) A<sup>1</sup>Π( $f$ )-X transition which led to an incorrect calculation of the Einstein  $A$  coefficient since Eq. (5) depends on the transition wavenumber. By applying the relevant  $e - f$  correction to each transition wavenumber, the Einstein coefficient was recalculated using Eq. (5) and the outputted dipole matrix elements. For transitions within the A<sup>1</sup>Π state this required some care due to many transitions being unaccounted for, as there exist potentially four transitions where LEVEL computes just one transition and thus one  $A$  coefficient that uses (often incorrect) transition information that LEVEL provided. For example, LEVEL gives Q-branch ( $\Delta J=0$ ) transitions within the same vibrational level a wavenumber of 0 cm<sup>-1</sup>, but in reality these correspond to long-wavelength, allowed  $\Lambda$ -doublet transitions between  $e$  and  $f$  states of the same rotational level. This meant calculating Eq. (5) in its entirety including determining the relevant Hönl-London factor (Hansson & Watson 2005). Note that these methods to recalculate the Einstein coefficient assume the expectation value of the DM/TDM function in Eq. (5) remains unchanged, which is in any case a common approximation used in other treatments and is unlikely to be problematic.

### 2.3 Final line lists

This above calculation procedure was followed for both <sup>12</sup>CH<sup>+</sup> and <sup>13</sup>CH<sup>+</sup> and line lists were generated considering states with  $J$  up to 68 and 69, respectively. For <sup>12</sup>CH<sup>+</sup> one further step was performed. The MARVEL energy levels with associated uncertainties were used to replace the ones computed by LEVEL.

Due to the greater accuracy of the empirical MARVEL data, calculated <sup>12</sup>CH<sup>+</sup> energies were replaced with the respective MARVEL values where available in the States file. These 'MARVELised' energy levels can be identified via the 'Label' column in the states file which indicates 'Ma' if the MARVEL energy level was used, or 'Ca' if there was no such available data. Note that the calculated energy prior to MARVELisation is given in the 'Calc.' column. The uncertainty in the States file is determined depending on the energy level used. For the MARVELised energies, the uncertainty provided by MARVEL was simply used. For the calculated energies (which includes all <sup>13</sup>CH<sup>+</sup> levels), an estimate for the uncertainty was made using the following expression:

$$\text{uncertainty} = av + bJ(J + 1) \quad (6)$$

where  $a = 0.05/0.1$  cm<sup>-1</sup> and  $b = 0.01/0.01$  cm<sup>-1</sup> for are constant parameters for the X<sup>1</sup>Σ<sup>+</sup>/A<sup>1</sup>Π electronic states, respectively. These parameters were estimated by analysing the evolution of <sup>12</sup>CH<sup>+</sup> obs. – calc. energy level residuals seen in Fig. 4, which plots the agreement of the MARVEL (obs.) and LEVEL (calc.) data and how this varies with  $v$  and  $J$  within each electronic state. Overall, the residuals were very small for low  $v$  and/or  $J$  levels of both the electronic states. Naturally, A<sup>1</sup>Π has greater residuals, especially for high  $v$ , since higher energies are probed and as a result of the manual treatment of  $\Lambda$ -doubling, but in general both states exhibit good accuracy. An apparent quadratic  $J$  dependence can be seen in the residuals in Fig. 4, motivating the form of Eq. (6).

## 3 RESULTS

### 3.1 Line list and File Structure

With calculated energies for rotational and vibrational levels of X<sup>1</sup>Σ<sup>+</sup> and A<sup>1</sup>Π, and transition frequencies and Einstein coefficients for allowed transitions, the components of the line list of CH<sup>+</sup> were complete. In accordance with ExoMol format, this was reformatted into a States and Transitions file (Tennyson et al. 2013), extracts from which for <sup>12</sup>CH<sup>+</sup> can be seen in Tables 3 and 4 respectively. The <sup>12</sup>CH<sup>+</sup> States file contains 1505 rovibrational energy levels covering the X<sup>1</sup>Σ<sup>+</sup> and A<sup>1</sup>Π electronic states up to a few thousand wavenumbers above the dissociation limit, additionally providing their uncertainty and associated quantum numbers defining the level. The Transitions file, characterising 34 194 transitions, contains Einstein  $A$  coefficients and frequencies for each allowed transition between the energy levels of the States file. For <sup>13</sup>CH<sup>+</sup> there are 1519 states and 42 387 transitions. We call these line lists PYT.

**Table 3.** Extract from the States file for  $^{12}\text{CH}^+$ .

$i$	Energy ( $\text{cm}^{-1}$ )	$g_i$	$J$	Unc. ( $\text{cm}^{-1}$ )	$\tau$ (s)	+/-	$e/f$	State	$v$	$\Lambda$	$\Sigma$	$\Omega$	label	Calc.
367	24005.218550	134	33	11.470000	1.1470E+01	-	e	X1Sigma+	5	0	0	0	Ca	24005.218550
368	24038.829766	10	2	0.610000	6.1000E-01	+	e	X1Sigma+	11	0	0	0	Ca	24038.829766
369	24072.559047	26	6	0.334901	3.3490E-01	-	f	A1Pi	0	1	0	1	Ma	24072.560989
370	24074.180657	26	6	0.217601	2.1760E-01	+	e	A1Pi	0	1	0	1	Ma	24074.148026
371	24091.232882	14	3	0.670000	6.7000E-01	-	e	X1Sigma+	11	0	0	0	Ca	24091.232882
372	24107.338107	78	19	4.250000	4.2500E+00	-	e	X1Sigma+	9	0	0	0	Ca	24107.338107
373	24131.807092	110	27	7.910000	7.9100E+00	-	e	X1Sigma+	7	0	0	0	Ca	24131.807092
374	24160.970652	18	4	0.750000	7.5000E-01	+	e	X1Sigma+	11	0	0	0	Ca	24160.970652
375	24162.245191	146	36	13.520000	1.3520E+01	+	e	X1Sigma+	4	0	0	0	Ca	24162.245191
376	24165.617170	166	41	17.320000	1.7320E+01	-	e	X1Sigma+	2	0	0	0	Ca	24165.617170
377	24229.503713	58	14	2.600000	2.6000E+00	+	e	X1Sigma+	10	0	0	0	Ca	24229.503713
378	24229.561434	30	7	0.366501	3.6650E-01	+	f	A1Pi	0	1	0	1	Ma	24229.563130
379	24231.703209	30	7	0.204901	2.0490E-01	-	e	A1Pi	0	1	0	1	Ma	24231.679179
380	24247.929131	22	5	0.850000	8.5000E-01	-	e	X1Sigma+	11	0	0	0	Ca	24247.929131
381	24351.966003	26	6	0.970000	9.7000E-01	+	e	X1Sigma+	11	0	0	0	Ca	24351.966003
382	24408.044035	34	8	0.354901	3.5490E-01	-	f	A1Pi	0	1	0	1	Ma	24408.042265

$i$ : State counting number,  $g_i$ : Total statistical weight,  $J$ : Total angular momentum, Unc: uncertainty ( $\text{cm}^{-1}$ ),  $\tau$ : lifetime (s), +/-: Total parity,  $e/f$ : Rotational parity,  $v$ : Vibrational level quantum number,  $\Lambda$ : Projection of electronic angular momentum,  $\Sigma$ : Projection of electron spin,  $\Omega$ : Projection of total angular momentum ( $\Omega = \Lambda + \Sigma$ ), Label: 'Ma' denotes MARVEL energy level, 'Ca' denotes LEVEL calculated energy level, Calc.: LEVEL calculated energy level value.

**Table 4.** Extract from the Transitions file for  $^{12}\text{CH}^+$ .

$f$	$i$	$A_{fi}$ ( $\text{s}^{-1}$ )	$\tilde{\nu}_{fi}$ ( $\text{cm}^{-1}$ )
516	377	3.1861E+01	2754.475947
1178	759	1.1669E-09	2755.165546
92	58	1.5055E+00	2756.287971
658	473	3.9484E+00	2756.308088
544	392	2.8961E+01	2756.981308
266	210	2.5046E+01	2757.306730
1169	754	5.0213E-09	2757.533295
1161	748	1.9419E-02	2757.544843
991	674	2.2755E-03	2757.621535
612	440	1.0042E+01	2758.338556
1166	751	1.6578E-09	2758.406401
186	141	1.7163E+01	2758.513693
1298	774	1.1399E+01	2758.878845

$f$ : Final state counting number,  
 $i$ : Initial state counting number,  
 $A_{fi}$ : Einstein  $A$  coefficient ( $\text{s}^{-1}$ ),  
 $\tilde{\nu}_{fi}$ : Transition wavenumber ( $\text{cm}^{-1}$ ).

It should be noted that, in the  $^{12}\text{CH}^+$  Transitions file, all A-A transitions involving vibrational levels with  $v \geq 4$  levels are excluded. This is due to further issues with LEVEL, which gave an error for these transitions. No A-A transitions have ever been detected and they are unlikely to be seen astronomically in the foreseeable future so this is not a significant defect.

### 3.2 Partition Functions

A partition function for  $^{12}\text{CH}^+$  was provided by [Barklem & Collet \(2016\)](#) for 42 temperatures up to 10000 K. The program ExoCross ([Yurchenko et al. 2018](#)) was used to calculate the partition function for both  $^{12}\text{CH}^+$  and  $^{13}\text{CH}^+$  in steps of 1 K up to 10000 K. The ExoMol convention, in accordance with HITRAN ([Gamache et al. 2017](#)), is to provide partition functions that include full atomic nuclear spin degeneracy,  $g_{ns}$ . For  $^{12}\text{C}^1\text{H}^+$ , this gives a value of 2, while for  $^{13}\text{CH}^+$  it gives 4. As such, the values of the  $^{12}\text{CH}^+$  partition function of Barklem and Collet, who do not account for this, have been multiplied by 2 for comparison, which can be seen in Fig. 5. Very good agreement can be seen below about 3000 K. At higher temperatures, agreement decreases somewhat which is likely due to the increasingly significant thermal occupation of higher energy electronic states that were not considered in this study, most notably the  $a^3\Pi$  state which lies between  $X^1\Sigma^+$  and  $A^1\Pi$ . As a result, a maximum temperature of 5000 K has been shown. JPL also provided a  $^{12}\text{CH}^+$  partition function for several low temperatures,



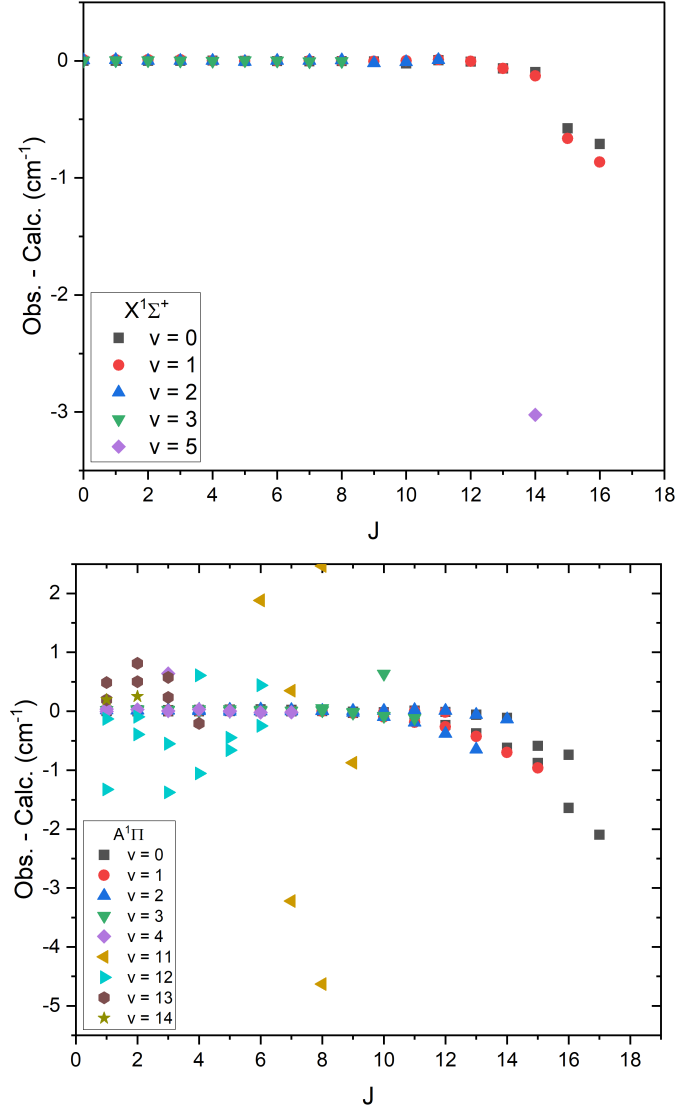


**Figure 4.** Obs. – Calc. residuals for the  $X^1\Sigma^+$  (Top) and  $A^1\Pi$  (Bottom) states for different vibrational levels as a function of  $J$ . Note that the two values for each  $(v, J)$  level in the  $A^1\Pi$  plot are the  $e$  and  $f$  parity states, split by  $\Lambda$ -doubling.

the largest of which, at 300 K, 30.7006 (Pickett et al. 1998) (again after accounting for nuclear spin degeneracy) shows excellent agreement with the calculated value here of 30.6990.

### 3.3 Spectra

Using the PYT  $^{12}\text{CH}^+$  line list, ExoCross (Yurchenko et al. 2018) was used to simulate absorption/emission spectra at various temperatures. Figure 6 shows simulated absorption spectra for temperatures of 296 K and 2000 K. A Doppler broadened Gaussian profile that is dependent on temperature has been used. The spectra have been separated with rotational and vibrational spectra in the top panel and electronic in the bottom, to avoid large gaps in the plot. Note that a logarithmic intensity scale has been used to show the relatively weak vibrational (IR) spectrum (seen for the wavenumber  $> 1000\text{ cm}^{-1}$  region of the top-panel plots) compared to the rotational and electronic spectrum. This corroborates the elusiveness of this spectrum as noted by previous studies.

To assess the quality of the calculated line list, comparison with previously recorded spectra are made. As no prior line list for  $\text{CH}^+$  exists, nor an experimental/observational spectrum covering an extensive wavelength range, comparison are made to selected portions of the full spectrum.

Low-lying pure rotational transitions of  $\text{CH}^+$  have been previously measured, as seen in Table 1, but no rotational spectra are presented. However, the JPL spectroscopy database (Pickett et al. 1998), who also aim to provide spectroscopic data for molecular transitions, used the first laboratory detection of the  $J = 1 - 0$   $\text{CH}^+$  rotational line (Pearson & Drouin 2006) along

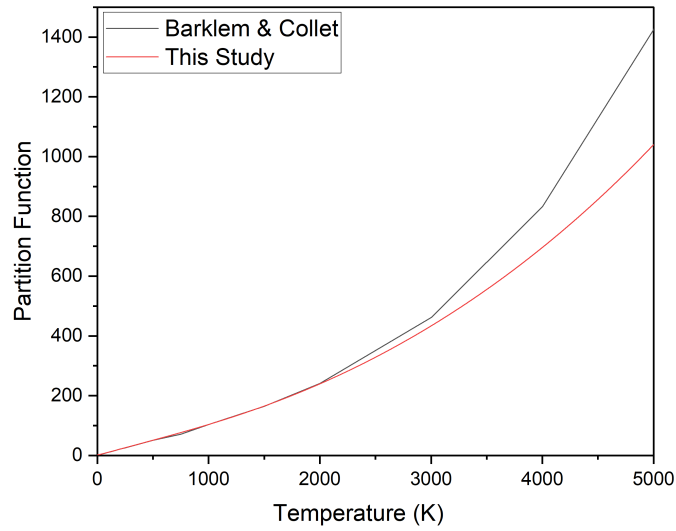


**Figure 5.**  $\text{CH}^+$  partition function as calculated from the line list by ExoCross compared with that of [Barklem & Collet \(2016\)](#).

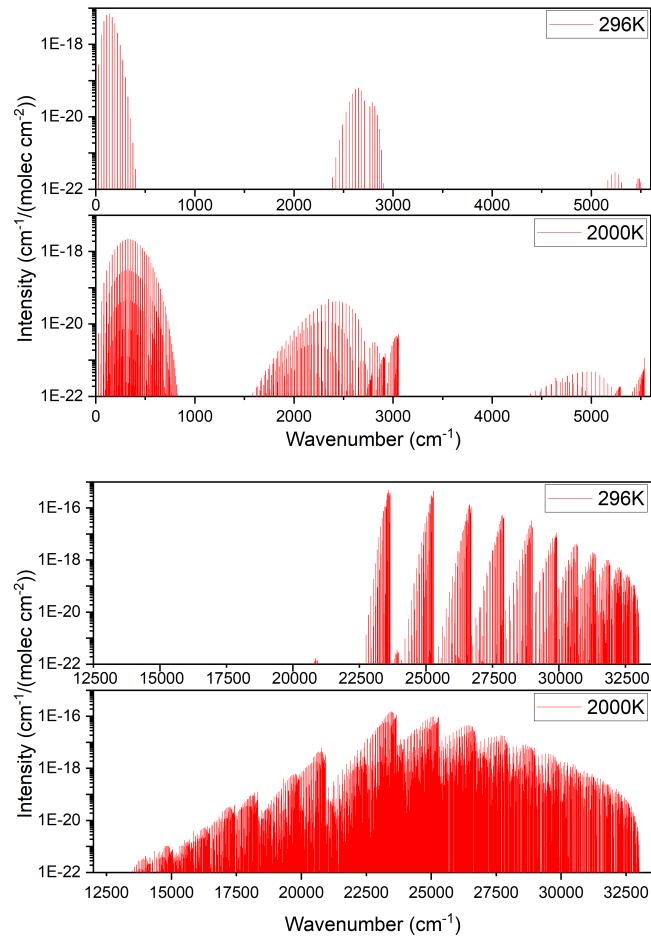


**Figure 6.** Simulated absorption spectra at 296 K and 2000 K, covering the rotational and vibrational (IR) bands (Top) and the electronic bands (Bottom). Spectra produced using a Doppler broadened profile with ExoCross.

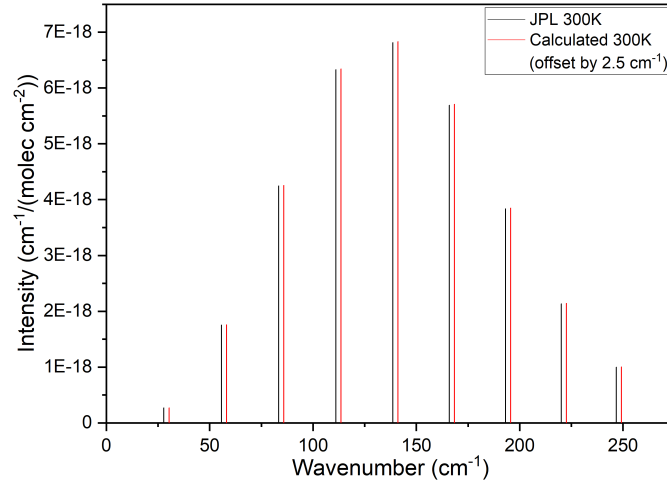


**Figure 7.** Comparison of the JPL  $\text{CH}^+$   $X^1\Sigma^+$  rotational spectrum (black) with the calculated rotational stick spectrum from this study (red). Note that the calculated data has been offset by  $2.5 \text{ cm}^{-1}$  for intensity comparison.

with previous electronic A-X band data to generate a predicted rotational spectrum up to  $J = 8$ . Although, as discussed previously, this laboratory detection was later found to be inaccurate by  $0.0019 \text{ cm}^{-1}$ , and a wider range of rotational lines have since been detected both in the lab and in space, JPL has not updated their database and the inaccurate data is still presented. Nevertheless, this discrepancy would not be visible on the scale of comparing multiple lines and their intensities should still be accurate, as such the JPL rotational spectrum of  $\text{CH}^+$  has been compared with the calculations of this study in Fig. 7. The simulated stick spectrum from ExoCross was run at a temperature of 300 K to match that of JPL, and the JPL intensities were converted to standard ExoMol/HITRAN units of  $\text{cm}/\text{molecule}$  for comparison. In Fig. 7, the calculated spectrum of this study has been offset by  $+2.5 \text{ cm}^{-1}$  to allow for visual comparison, as the wavenumbers agree to a high degree of accuracy. The intensities can also be seen to agree closely.

The weak nature of the vibrational (IR) spectrum of  $\text{CH}^+$  means it has only been detected in one astrophysical object (Neufeld et al. 2021) and one laboratory study (Domenech et al. 2018), of which no presented spectra exist, so visual comparison cannot be made. The A-X electronic spectrum is by far the most studied of  $\text{CH}^+$  with many experimental studies focusing on the molecule, however, presented spectra are limited. A study by Grieman et al. (1981) used laser-induced fluorescence to probe  $\text{CH}^+$  emission and presented a portion of the  $v = 0 - 0$  band of the A-X spectrum, a comparison to which, using a simulated emission spectrum, has been shown in Fig. 8. The previous study also gave arbitrary intensity units and is probably not recorded in sample in thermodynamic equilibrium, so the intensity pattern is not expected to match that of this study. As such, a temperature of 2500 K was somewhat arbitrarily chosen for our calculated spectrum based on the high temperature requirement and certain similarities in intensity pattern. On Fig. 8, the intensity units correspond only to the results of this study (red). The spectrum from the previous study had to be offset slightly to match the spectrum of this study which indicates a slight error in their axes, since the transition wavenumbers of the two studies match to a high degree of accuracy.

$\text{CH}^+$  A-X absorption was seen in diffuse interstellar bands (DIBs) along the line of sight towards star system Herschel 36 and three lines were detected (York et al. 2013), R(0), R(1) and Q(1). A comparison to the spectra of these is shown in Fig. 9. Note that since the study used wavelength units for their spectrum, wavenumber increases right to left. Upon analysis, the DIBs were observed to be blueshifted relative to the calculated lines with an offset of approximately  $+6.75 \text{ cm}^{-1}$  ( $-1.21 \text{ \AA}$ , indicating the absorbing object is moving at  $85.7 \text{ km s}^{-1}$  towards us). After matching the line positions, an offset of  $+2 \text{ cm}^{-1}$  (to the left) was applied to the DIB data to allow for visual comparison of the intensities. The red intensity units correspond to calculated data, while the black relative flux units correspond to the DIB study. Since the temperature of the absorption region was not found in the previous study, spectra were simulated at various temperatures using ExoCross to match up the intensity pattern of the observed lines, which would be expected to agree between these two studies. It appears that a temperature of 18 K matches the  $J = 1$  lines well (by eye) while overestimating the observed  $J = 0$  line flux. A temperature higher than 18 K results in an intensity decrease from  $J = 0$  levels but an increase from  $J = 1$  levels (it is assumed that thermal population of a rotational level is proportional to the intensity of transitions from that level). Thus the intensity of the  $J = 0$  and  $J = 1$  lines on the above spectra cannot both match up. This suggests that the region is consistent with a temperature of 18 K, but that the observed  $J = 0$  line is optically thick, and thus is limited in its intensity.

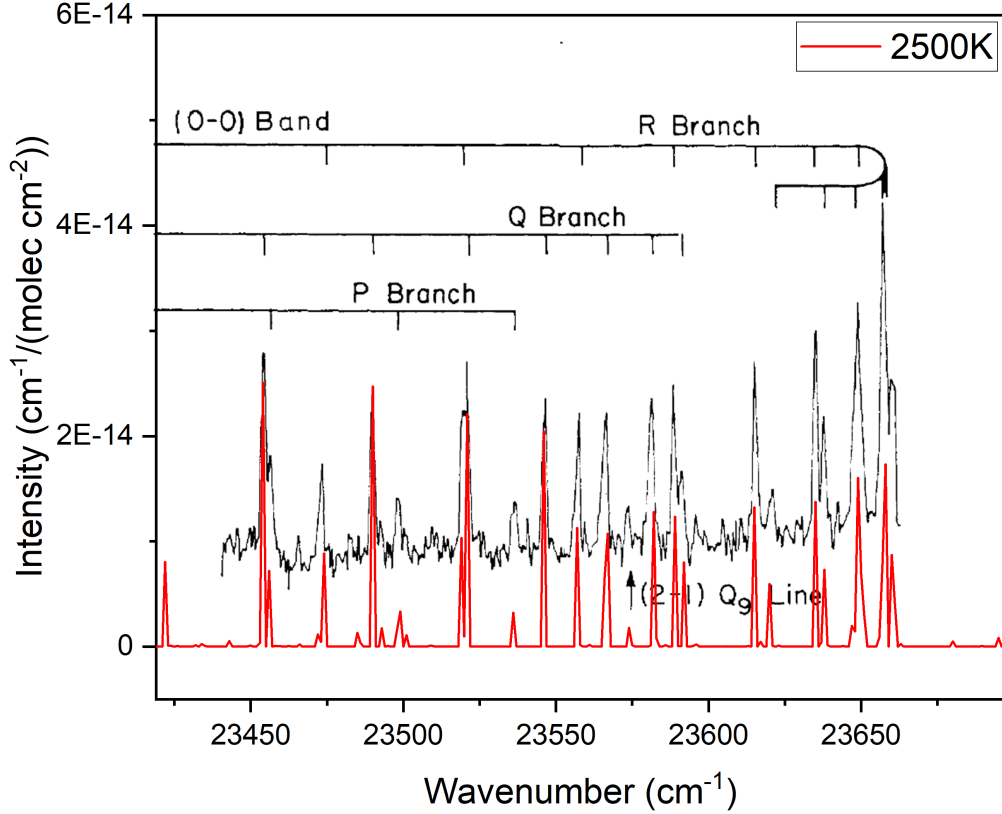


**Figure 8.** Comparison of the  $v = 0 - 0$   $A^1\Pi - X^1\Sigma^+$  band spectrum from [Grieman et al. \(1981\)](#) (black) with the simulated emission spectrum from ExoCross at 2500K (red). A Doppler line profile was used. The intensity scale corresponds only to the calculated ExoCross data, since Grieman et al. provided arbitrary units.

**Table 5.** Comparison of Einstein A coefficients for the  $v = 1 - 0$  band of  $X^1\Sigma^+$  from [Changala et al. \(2021\)](#) to those of this study.

Transition	Changala et al.	This Study	Transition	Changala et al.	This Study	Transition	Changala et al.	This Study
R(19)	2.88283	3.03821	R(5)	0.09044	0.06712	P(9)	4.09076	3.93378
R(18)	2.41605	2.55795	R(4)	0.18326	0.14975	P(10)	4.37871	4.21857
R(17)	1.98722	2.11561	R(3)	0.30131	0.25858	P(11)	4.65704	4.49416
R(16)	1.59804	1.71294	R(2)	0.43506	0.38462	P(12)	4.9231	4.75791
R(15)	1.24991	1.35135	R(1)	0.56372	0.50836	P(13)	5.17457	5.00751
R(14)	0.94394	1.03198	R(0)	0.61818	0.56547	P(14)	5.40944	5.24094
R(13)	0.68091	0.75564	P(1)	2.87367	2.67911	P(15)	5.62596	5.45643
R(12)	0.46122	0.52277	P(2)	2.28988	2.14908	P(16)	5.82263	5.65251
R(11)	0.28493	0.33346	P(3)	2.41302	2.27697	P(17)	5.99824	5.82790
R(10)	0.15172	0.18743	P(4)	2.64446	2.50664	P(18)	6.15178	5.98161
R(9)	0.06085	0.08400	P(5)	2.91483	2.77344	P(19)	6.2825	6.11286
R(8)	0.01117	0.02207	P(6)	3.20295	3.05749	P(20)	6.38985	6.22109
R(7)	0.00108	0.00009	P(7)	3.49882	3.34926			
R(6)	0.02845	0.01601	P(8)	3.79625	3.64282			

### 3.4 Einstein Coefficients

Einstein  $A$  coefficients can be compared with the work of [Changala et al. \(2021\)](#) who analysed unusual  $\text{CH}^+$  rovibrational emission patterns in NGC 7027 and gave Einstein coefficients for R- and P- branch transitions in the  $v = 1 - 0$  X-X band in an attempt to explain unexpectedly weak R-branch transitions. The calculated coefficients of this study have been compared with these in Table 5 and Figure 10. For plotting, a parameter  $m$  has been used, positive  $m$  values indicate R-branch transitions, and negative ones indicate P-branch transitions, originating from the rotational state  $J = m$ . The Einstein coefficients are seen to agree well, which supports the observation of weaker R-branch transitions. [Changala et al. \(2021\)](#) also used PECs from [Cho & Le Roy \(2016\)](#), so the differences in results likely lies with differences in fitting, or the differing dipole moments used. Despite this, since the DMs for these vibrational transitions are so small (hence the weakness of the observed transitions), the level of disagreement between results is unproblematic.

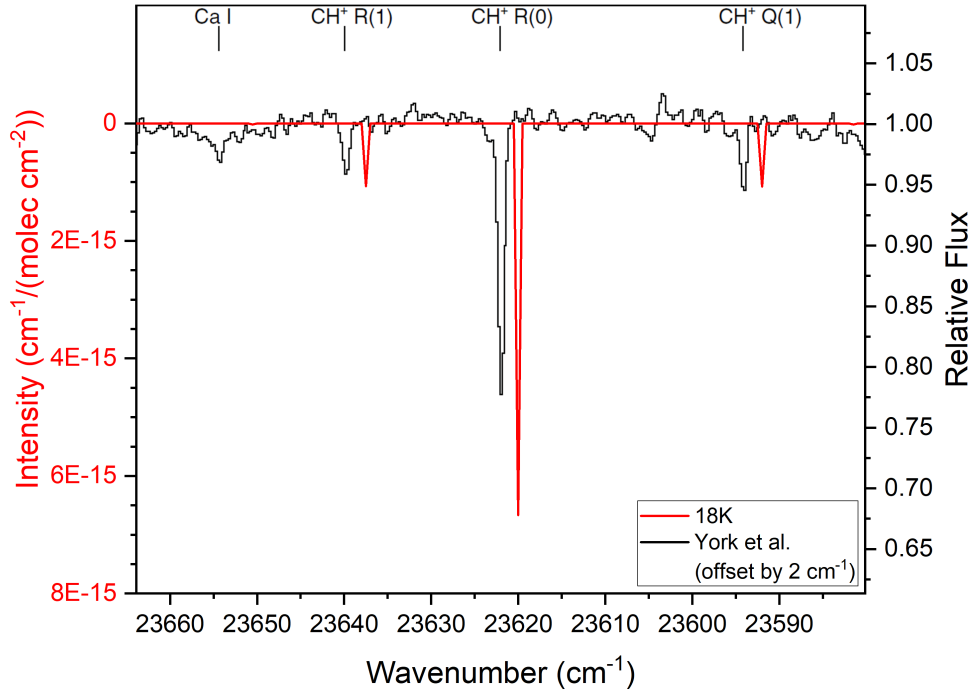


**Figure 9.** Comparison of the A-X spectral lines of the diffuse interstellar bands (DIBs) observed towards Herschel 36 (black) (York et al. 2013) with the simulated absorption spectrum of this study at 18 K (red), for which a Doppler line profile is used. The red units on the left axis correspond to the calculated data of this study, while the black units on the right correspond to the intensity units provided by the DIB study. Note that wavenumber increases right to left as the original DIB study used wavelength units. The DIB data was originally blueshifted by  $\sim +6.75 \text{ cm}^{-1}$  ( $-1.21 \text{ \AA}$ ), after aligning the two spectra the DIB data was offset by  $+2 \text{ cm}^{-1}$  (to the left) for clearer intensity comparison.

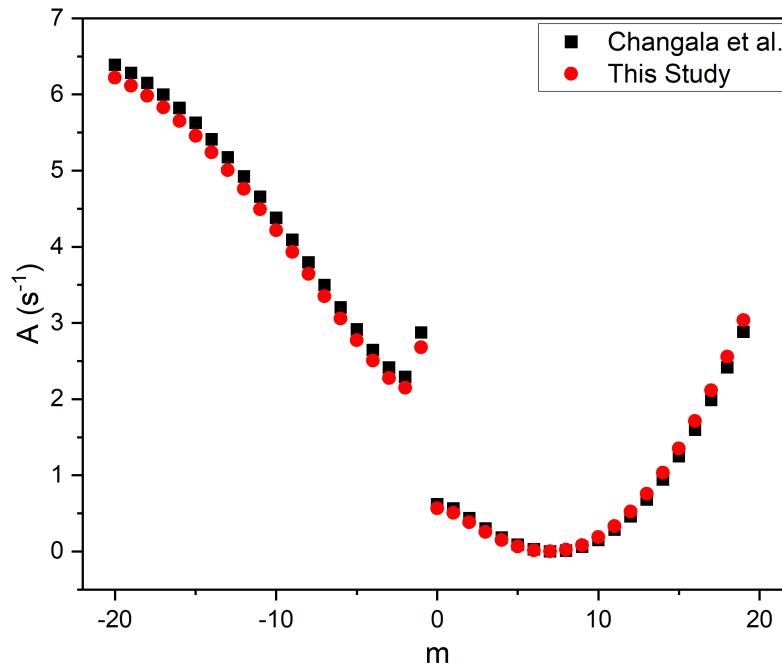


**Figure 10.** Comparison of Einstein coefficients for the  $v = 1 - 0$  band of  $\text{X}^1\Sigma^+$  from Changala et al. (2021) with those calculated in this study. P and R-branch transitions have been organised into a parameter  $m$  for plotting, where the value of  $m$  indicates the (lower state) rotational quantum number of the transition, and the  $\pm$  indicates R/P-branch respectively

#### 4 DISCUSSION & CONCLUSIONS

A rovibronic line list has been calculated for the  $X^1\Sigma^+$  and  $A^1\Pi$  states of  $^{12}\text{CH}^+$  and  $^{13}\text{CH}^+$  for the first time; the PYT line lists provide energy levels with uncertainties, transition frequencies and Einstein  $A$  coefficients. The states, transition and partition function files for the PYT line lists can be downloaded from [www.exomol.com](http://www.exomol.com) or zenodo.

The line list is used to generate absorption and emission spectra, as well as partition functions, which help to visualise the line list and provide a comparison to previous studies. The  $^{12}\text{CH}^+$  line list is naturally very accurate for  $v = 0 - 3$  of both states where empirical energy levels are comprehensive. The calculated levels, making up the line list outside the realm of observational data, are more uncertain but our analysis shows that the calculations reproduce experimental line frequencies well (to  $\lesssim 0.01 \text{ cm}^{-1}$ ) up to at least  $J = 12$  for  $X^1\Sigma^+$  and  $A^1\Pi(f)$  states. Residuals in  $A^1\Pi(e)$  states are expectedly larger than their  $f$  counterparts since their energies were calculated with an approximate treatment of  $\Lambda$ -doubling. These show still accuracies to at least  $\sim 0.01 \text{ cm}^{-1}$  for  $J \leq 9$ ; however, the lack of observational data for  $v \geq 4$  means these data should be treated with more caution. In general, agreement is better in the lower energy  $X^1\Sigma^+$ , as expected, and in both states residuals increase with greater  $v$  and exhibit an apparent  $J^2$  dependence at high  $J$ . Such levels are high in energy (for example the lowest  $A^1\Pi$  level is over  $23\,600 \text{ cm}^{-1}$  above that of  $X^1\Sigma^+$ ) meaning that the discrepancy is likely due, in part, to interaction with more highly excited electronic states that has not been considered here, such as spin-orbit coupling, which becomes increasingly important at higher energies and may perturb energy levels. Note that, where residuals are relatively large, the MARVEL (obs.) data is also more uncertain, since these high-energy levels are typically determined by just one observed transition (usually multiple are available) yielding uncertainties of the order  $1 - 3 \text{ cm}^{-1}$  for the few  $v \geq 4$  empirical levels in both  $X^1\Sigma^+$  and  $A^1\Pi$  states.

The PYT line lists for  $^{12}\text{C}^1\text{H}^+$  and  $^{13}\text{C}^1\text{H}^+$  comprehensively characterises well above and beyond the domain of previous observation. Identification of future avenues of research, dependent on later observation, have also been presented. The accuracy and completeness of the line list open up its potential application to future high-resolution studies and any hot observations of  $\text{CH}^+$ , as well as the investigation of a range of astronomical environments, including the complex chemistry of interstellar clouds.

#### ACKNOWLEDGMENTS

This work was supported by the European Research Council (ERC) under the European Union's Horizon 2020 research and innovation programme through Advance Grant number 883830 and the STFC Projects No. ST/M001334/1 and ST/R000476/1. We thank Nike Dattani for providing the copy of LEVEL which we adapted for this study.

#### DATA AVAILABILITY

The states, transition and partition function files for the  $^{12}\text{CH}^+$  and  $^{13}\text{CH}^+$  line lists can be downloaded from [www.exomol.com](http://www.exomol.com) and zenodo. Inputs for LEVEL, and the  $^{12}\text{CH}^+$  MARVEL energies and transitions files are provided as supplementary data to this article. ExoCross and our adapted version of LEVEL are available at [github.org/exomol](https://github.org/exomol).

#### REFERENCES

- Amano T., 2010a, *J. Chem. Phys.*, 133, 244305  
 Amano T., 2010b, *ApJL*, 716, L1  
 Amano T., 2015, in Simos T. E., Maroulis G., eds, AIP Conference Proceedings Vol. 1642, Proceedings of the International Conference of Computational Methods in Sciences and Engineering 2010 (ICCMSE-2010). pp 317–320, doi:10.1063/1.4906682  
 Amano T., Pearson J., Drouin B., Yu S., 2015.  
 Babb J. F., McLaughlin B. M., 2017, *MNRAS*, 468, 2052  
 Barinovs G., van Hemert M. C., 2004, *Chem. Phys. Lett.*, 399, 406  
 Barklem P. S., Collet R., 2016, *A&A*, 588, A96  
 Bembenek Z., 1997, *J. Mol. Spectrosc.*, 181, 136  
 Bembenek Z., Cisak H., Kepa R., 1987, *J. Phys. B: At. Mol. Opt. Phys.*, 20, 6197  
 Biglari Z., Shayesteh A., Maghari A., 2014, *Computational and Theoretical Chemistry*, 1047, 22  
 Botterud I., Lofthus A., Veseth L., 1973, *Physica Scripta*, 8, 218  
 Carrington A., Ramsay D. A., 1982, *Physica Scripta*, 25, 272  
 Carrington A., Softley T. P., 1986, *Chem. Phys.*, 106, 315  
 Cernicharo J., Liu X. W., GonzalezAlfonso E., Cox P., Barlow M. J., Lim T., Swinyard B. M., 1997, *ApJ*, 483, L65  
 Chakrabarti K., Dora A., Ghosh R., Choudhury B. S., Tennyson J., 2017, *J. Phys. B: At. Mol. Opt. Phys.*, 50, 175202  
 Changala P. B., Neufeld D. A., Godard B., 2021, *ApJ*, 917, 16  
 Cho Y.-S., Le Roy R. J., 2016, *J. Chem. Phys.*, 144, 024311  
 Cosby P. C., Helm H., Moseley J. T., 1980, *ApJ*, 235, 52

- Crane P., Lambert D. L., Sheffer Y., 1995, *ApJS*, 99, 107
- Crawford I. A., 1989, *MNRAS*, 241, 575
- Dalgarno A., 1976, in Burke P. G., Moiseiwitsch B. L., eds., *Atomic Processes and Application*. Elsevier, pp 109–132, doi:10.1016/B978-0-7204-0444-9.50010-7
- Domenech J. L., Jusko P., Schlemmer S., Asvany O., 2018, *ApJ*, 857, 61
- Douglas A., Herzberg G., 1942, *Can. J. Phys.*, 20, 71
- Douglas A. E., Morton J. R., 1960, *ApJ*, 131, 1
- Dubois I., Lefebvre P. H., 2004, *Mol. Phys.*, 102, 23
- Dunham T., 1937, *PASP*, 49, 26
- Falgarone E., et al., 2010, *A&A*, 521, L15
- Falgarone E., et al., 2017, *Nature*, 548, 430
- Faure A., et al., 2017, *MNRAS*, 469, 612
- Furtenbacher T., Császár A. G., Tennyson J., 2007, *J. Mol. Spectrosc.*, 245, 115
- Gamache R. R., et al., 2017, *J. Quant. Spectrosc. Radiat. Transf.*, 203, 70
- Gao Y., Wu T., Wan M., 2017, *Computational and Theoretical Chemistry*, 1117, 276
- Godard B., Pineau des Forêts G., Hennebelle P., Bellomi E., Valdivia V., 2023, *A&A*, 669, A74
- Gredel R., 1997, *A&A*, 320, 929
- Gredel R., Van Dishoeck E. F., Black J. H., 1993, *A&A*, 269, 477
- Grieman F. J., Mahan B. H., O’Keefe A., Winn J. S., 1981, *Faraday Discussions*, 71, 191
- Hakalla R., Kępa R., Szajna W., Zachwieja M., 2006, *Eur. Phys. J. D*, 38, 481
- Hakalla R., Kępa R., Szajna W., Zachwieja M., 2007, *Acta Physica Polonica A*, 111, 821
- Hansson A., Watson J. K. G., 2005, *J. Mol. Spectrosc.*, 233, 169
- Hechtfisher U., Williams C., Lange M., Linkemann J., Schwalm D., Wester R., Wolf A., Zajfman D., 2002, *J. Chem. Phys.*, 117, 8754
- Hechtfisher U., Rostas J., Lange M., Linkemann J., Schwalm D., Wester R., Wolf A., Zajfman D., 2007, *J. Chem. Phys.*, 127, 204304
- Helm H., Cosby P. C., Graff M. M., Moseley J. T., 1982, *Phys. Rev. A*, 25, 304
- Hobbs L. M., Thorburn J. A., Oka T., Barentine J., Snow T. P., York D. G., 2004, *ApJ*, 615, 947
- Kanzler A. W., Sun H. S., Freed K. F., 1991, *Int. J. Quantum Chem.*, 39, 269
- Kowalski K., Piecuch P., 2001, *Chem. Phys. Lett.*, 347, 237
- Krelowski J., Galazutdinov G. A., Bondar A., 2020, *Astronomische Nachrichten*, 341, 56
- Le Roy R. J., 2017, *J. Quant. Spectrosc. Radiat. Transf.*, 186, 167
- Mbiba Touedebe C., Nkem C., Owono Owono L. C., 2023, *Mol. Phys.*, 121, e2151946
- Mueller H. S. P., 2010, *A&A*, 514, L6
- Muller S., et al., 2017, *A&A*, 606, A109
- Naylor D. A., et al., 2010, *A&A*, 518, L117
- Neufeld D. A., Godard B., Changala P. B., Faure A., Geballe T. R., Guesten R., Menten K. M., Wiesemeyer H., 2021, *ApJ*, 917, 15
- Pearson J. C., Drouin B. J., 2006, *ApJ*, 647, L83
- Pickett H. M., Poynter R. L., Cohen E. A., Delitsky M. L., Pearson J. C., Müller H. S. P., 1998, *J. Quant. Spectrosc. Radiat. Transf.*, 60, 883
- Rangwala N., et al., 2011, *ApJ*, 743, 94
- Ritchey A. M., Welty D. E., Dahlstrom J. A., York D. G., 2015, *ApJ*, 799, 197
- Sarre P. J., Walmsley J. M., Whitham C. J., 1986, *J. Chem. Soc. Faraday Trans. II*, 82, 1243
- Sarre P. J., Whitham C. J., Graff M. M., 1989, *J. Chem. Phys.*, 90, 6061
- Sauer S. P. A., Spirko V., 2013, *J. Chem. Phys.*, 138, 024315
- Saxon R. P., Kirby K., Liu B., 1980, *J. Chem. Phys.*, 73, 1873
- Tennyson J., Yurchenko S. N., 2012, *MNRAS*, 425, 21
- Tennyson J., Hill C., Yurchenko S. N., 2013, in *6<sup>th</sup> international conference on atomic and molecular data and their applications ICAMDATA-2012*. AIP, New York, pp 186–195, doi:10.1063/1.4815853
- Thi W. F., et al., 2011, *A&A*, 530, L2
- Valdivia V., Godard B., Hennebelle P., Gerin M., Lesaffre P., Le Boulot J., 2017, *A&A*, 600, A114
- Vidal-García A., et al., 2022, in *EPJ Web of Conferences*.
- Wesson R., et al., 2010, *A&A*, 518, L144
- York D. G., et al., 2013, *Proc. International Astronomical Union*, 9, 89
- Yu S., Drouin B. J., Pearson J. C., Amano T., 2018, *J. Mol. Spectrosc.*, 350, 30
- Yurchenko S. N., Al-Refaie A. F., Tennyson J., 2018, *A&A*, 614, A131